



Defect and interface engineering of hexagonal $\text{Fe}_2\text{O}_3/\text{ZnCo}_2\text{O}_4$ n-n heterojunction for efficient oxygen evolution reaction

Shaqi Fu^a, Yiran Ma^c, Xuechun Yang^a, Xuan Yao^a, Zheng Jiao^{b,*}, Lingli Cheng^{a,*}, Pandeng Zhao^{a,*}

^a School of Environmental and Chemical Engineering, Shanghai University, Shanghai 200444, PR China

^b Shanghai Applied Radiation Institute, Shanghai University, Shanghai 201800, PR China

^c CPU Hydrogen Power Technology (Suzhou) Co., Ltd, 215000, PR China

ARTICLE INFO

Keywords:

N-n heterojunction
Interface engineering
Oxygen vacancy
Defect
OER

ABSTRACT

This work aimed at constructing defective heterojunction to optimize the electronic structure and exploring the intrinsic mechanism of its excellent electrocatalytic performance. Specifically, Fe^{6+} is introduced through the cation exchange method using hexagonal interpenetrating twin Zn/Co -ZIFs as precursors. Then, the n-n heterojunction featuring oxygen vacancies at the biphasic interface of Fe_2O_3 and ZnCo_2O_4 is constructed through calcination. The obtained electrode for oxygen evolution reaction (OER) only requires 261 mV overpotential to achieve a current density of 10 mA cm^{-2} , and shows exceptional stability at high current density, lasting for 50 h. Density functional theory calculations confirm that the construction of heterojunction can effectively optimize the d-band center and improve the adsorption of the active center on oxygen-containing intermediates, thus optimizing the Gibbs free energy of the OER. This study provides inspiration and interface engineering strategy for the design of highly active catalysts, and enhances our understanding of the OER mechanism.

1. Introduction

The oxygen evolution reaction (OER) is expected to solve the future energy crisis owing to its good performance in various applications such as fuel cells, hydrogen fuel, and metal-air cells [1,2]. However, the efficiency of the OER in alkaline electrolytes is hindered by kinetic retardation and excessive overpotential [3,4]. Although IrO_2 and RuO_2 are currently the most effective catalysts for the OER, their high cost and scarcity hinder their large-scale application [5]. Therefore, various transition metal oxides have attracted significant interest as alternative catalysts [6–8]. However, most of them suffer from poor electrical conductivity and stability, which considerably limits their application as OER electrocatalysts.

Structural modifications have the potential to enhance the stability of these catalysts while also creating additional active sites. Among these modifications, hollow structures featuring independent and sturdy frameworks are particularly promising candidates [9,10]. For instance, Ren and co-workers reported that CoFe -Hydroxide hollow nanocages exhibit superior OER performance, with an overpotential of 274 mV at 10 mA cm^{-2} . Its unique hollow structure not only improves the

utilization efficiency of internal metal atoms but also promotes mass transfer at the interface between the electrolyte and active atoms [11]. Xia and co-workers reported hollow porous $\text{Co}_3\text{O}_4/\text{CoMoO}_4$ hybrids displays ultralow overpotential. This unique hollow porous structure exposes more active sites and shortens the diffusion distance from the electrolyte to the active center [12]. Nevertheless, the construction of unique hollow structures using MOFs remains complex.

As for the poor electrical conductivity of metal oxides, it is proved that the introduction of oxygen vacancies (O_v) can promote the adsorption of OH^- on the electrocatalyst surface, and optimize its electronic structure. Thus, the conductivity can be enhanced and the kinetic performance of OER can be improved [13,14]. Effective methods to obtain O_v include reduction treatment, heat treatment, plasma treatment, and anion/cation doping [15]. For example, Zhu's group synthesized oxygen-defective $\text{Fe}_2\text{O}_3/\text{CoO}_x$ nanorod array composite films via annealing in an oxygen-deficient atmosphere, resulting in the creation of numerous active sites [13]. Wang's group proposed a Ni foam-supported $\text{Co}_3\text{O}_4/\text{Co}_3\text{S}_4$ with rich O and S dual vacancies. O_v optimizes the electron distribution on the surface and reduces the adsorption energy barrier of OH^* radicals [16]. However, metal oxides

* Corresponding authors.

E-mail addresses: zjiao@shu.edu.cn (Z. Jiao), chenglingli@t.shu.edu.cn (L. Cheng), tengteng87@shu.edu.cn (P. Zhao).

<https://doi.org/10.1016/j.apcatb.2023.122813>

Received 16 January 2023; Received in revised form 19 April 2023; Accepted 24 April 2023

Available online 25 April 2023

0926-3373/© 2023 Elsevier B.V. All rights reserved.

containing O_V are easily oxidized during the OER process, resulting in degraded performance [17]. Thus, it is evident that further research and development are required to synthesize metal oxides that exhibit exceptional activity and stability.

Recent studies have demonstrated that interfacial engineering can effectively modulate surface properties. This increases the charge transfer rate at the interface and facilitates the adsorption of reaction intermediates [18,19]. For instance, Zheng et al. [20] demonstrated that a $UCoO_4/Co_3O_4$ heterojunction was formed with high catalytic performance and excellent long-term electrolytic stability during the OER. A low overpotential (280 mV) was shown at a current density of 10 mA cm^{-2} . Li et al. [21] reported a novel hollow $CoO/Co_4S_3 @CoO/Co_4S_3$ heterojunction with a core-shell structure. The O-Co-S bond at the heterojunction interface enhances the intrinsic activity of the CoO active sites in the OER. Nevertheless, the construction of heterogeneous interfaces is usually complex and difficult on a large scale, which severely limits their practical application. Recently, increasing attention has been paid to the active phase and dynamic evolution during the OER. Li et al. [22] found that the interfacial effect between NiFe LDH and FeOOH accelerates the charge transfer and thus facilitates the formation of β -Ni(Fe)OOH intermediates with high intrinsic activity. Nowadays, there has been a growing interest in understanding the intrinsic mechanism of catalysis, which is crucial for the development and design of highly active catalysts.

To solve the aforementioned problems, $Fe^{\delta+}$ is introduced through the cation exchange method using hexagonal interpenetrating twin Zn/Co-ZIFs as precursors. Hexagonal star-shaped $Fe_2O_3/ZnCo_2O_4$ with both O_V and n-n heterojunction is obtained. The hexagonal star-shaped ZIF skeleton provides superior structural stability, while its unique hollow structure enhances the specific surface area. The introduction of $Fe^{\delta+}$ causes a decrease in crystallinity, resulting in distortion of the electronic domains around the Zn/Co metal and the introduction of more O_V . Conventional characterizations are used to elaborate on the interfacial electron transfer mechanism. The formation of n-n heterojunction at the $Fe_2O_3/ZnCo_2O_4$ biphasic interface is confirmed, which enhances the intrinsic activity of the active site. The turnover frequency of $Fe_2O_3/ZnCo_2O_4$ is 4.4 times higher than that of $ZnCo_2O_4$, indicating excellent intrinsic activity. Through the use of density functional theory calculations, the underlying intrinsic mechanism responsible for the improvement of OER performance by constructing heterogeneous structures containing O_V is elucidated, with the aim of enhancing our understanding of the OER mechanism and catalyst design.

2. Materials and Methods

2.1. Materials

All chemicals, including cobalt dihydrate acetate ($Co(CH_3COO)_2 \cdot 2H_2O$, AR), zinc dihydrate acetate ($Zn(CH_3COO)_2 \cdot 2H_2O$, AR), 2-methylimidazole (2-MeIM, 98%), cetyltrimethylammonium bromide (CTAB, $\geq 99\%$), Iron(II) chloride tetrahydrate ($FeCl_2 \cdot 4H_2O$, AR), methanol (CH_3OH , $\geq 99.5\%$) and absolute ethanol (CH_3CH_2OH , $\geq 99.7\%$), all purchased from Sinopharm Chemical Reagent Co.

2.2. Synthesis of Zn_xCo_{1-x} -ZIF

First, 1 mmol $Zn(CH_3COO)_2 \cdot 2H_2O$, 0.5 mmol $Co(CH_3COO)_2 \cdot 2H_2O$ and 0.33 mmol CTAB were dissolved in 38 mL of deionized water (DIW) to prepare solution A, and 30 mmol 2-MeIM was dissolved in 38 mL of DIW to prepare solution B. Solution A was quickly poured into solution B and stirred. Then, the solution was transferred into 100 mL Polytetrafluoroethylene reactor and subjected to a hydrothermal reaction at 120 °C for 24 h in an oven. Subsequently, the solution was washed with methanol and ethanol for several times, followed by drying in a vacuum oven at 60 °C for 12 h. The $Zn_1Co_{0.5}$ -ZIF precursor was prepared. A series of Zn_xCo_{1-x} -ZIF precursors were prepared by varying the ratio of Zn

(CH_3COO) $_2 \cdot 2H_2O$ and $Co(CH_3COO)_2 \cdot 2H_2O$ in the supporting information (ESI) (Table S1).

2.3. Synthesis of FeZnCo hydroxide-X and Fe-precursor

150 mg of $Zn_1Co_{0.5}$ -ZIF precursor was dissolved in MeOH (10 mL) and sonicated for 15 min called solution A. Thereafter, 300 mg of $FeCl_2 \cdot 4H_2O$ was dissolved in 15 mL of methanol called solution B. Solution B was quickly poured into solution A and stirred at 20–25 °C for 1 h. After centrifugation and washing, the solution was dried in a vacuum oven at 60 °C for 12 h to obtain FeZnCo Hydroxide. A series of FeZnCo Hydroxide-X samples with different degrees of $Fe^{\delta+}$ exchange were prepared by controlling the stirring time (X = 10 min, 30 min, and 2 h). The experimental conditions for the preparation of the Fe-precursor were kept constant, except for $Zn_1Co_{0.5}$ -ZIF.

2.4. Synthesis of $Fe_2O_3/ZnCo_2O_4$, $ZnCo_2O_4$ and Fe_2O_3

25 mg of FeZnCo-LDH, $Zn_1Co_{0.5}$ -ZIF, and Fe-precursor, were calcined in a tube furnace at 300 °C for 2 h, respectively. The heating rate was maintained at 5 °C/min with air, and upon cooling to room temperature, the final products obtained were $Fe_2O_3/ZnCo_2O_4$, $ZnCo_2O_4$, and Fe_2O_3 .

2.5. Characterization

The morphology and structure of the prepared composites were characterized by field emission scanning electron microscopy (SEM), and transmission electron microscopy (TEM). The characterization of the crystal structure was performed by X-ray diffraction (XRD) equipped with a Cu-K α radiation ($\lambda = 1.5406 \text{ \AA}$) source in the test range $2\theta = 5\text{--}80^\circ$. Raman spectra were obtained on an *inVia Qontor/Renishaw inVia Qontor confocal microscope using 532 nm as the laser. Brunauer-Emmett-Teller (BET) surface area and pore size distribution were performed by N_2 adsorption-desorption isotherms using a Quadrasorb SI instrument at 77 K. X-ray photoelectron spectroscopy (XPS, Thermo Scientific ESCALAB 250 XI) used to analyze the chemical state of the sample surfaces. The band gap of the samples was performed by UV-Vis spectroscopy (Shimadzu 1700). Electron Paramagnetic Resonance (EPR) measurements were performed at room temperature on an X-band EPR spectrometer (Bruker EMX PLUS) at 573k.

2.6. Electrochemical measurements

To prepare the catalyst, 3 mg of the catalyst was mixed with 165 μ L of DIW, 55 μ L of ethanol, and 20 μ L of Nafion solution. The resulting mixture was sonicated for 30 min until the catalyst was uniformly dispersed. Then, 80 μ L of the mixture was applied onto a nickel foam with a coating area of $1 \times 1 \text{ cm}^2$ and dried in a vacuum oven at 25 °C for 2 h. Metrohm Autolab B.V. was chosen as the electrochemical measurement device.

The catalyst activity tests were performed in a typical three-electrode electrolyzer containing 1 M KOH electrolyte solution (25 °C). The prepared electrode (working electrode), Hg/HgO electrode (reference electrode), and a carbon rod (counter electrode) were connected to a Metrohm Autolab B.V. for electrochemical testing. The measured potential is called the reversible hydrogen electrode (RHE), and its formula is $E_{RHE} = E_{Hg/HgO} + 0.098 + 0.059 \times pH$ ($pH=14$). The electrodes were activated by cycling 50 times at a scan rate of 50 mV s^{-1} . Cyclic voltammetric (CV) curves were measured at a scan rate of 5 mV s^{-1} to evaluate the catalytic OER performance. All linear sweep voltammograms (LSV) tests with 90% i_R were corrected. The bilayer capacitance (C_{dl}) values were determined from the CV curves at scan rates of 0–0.1 V. The electrochemical impedance spectra (EIS) were 0.6 V for all the catalysts in the 100 kHz–0.01 Hz range. The in-situ impedance was obtained in the voltage interval 0–0.6 V. More details on the

experiments and Density functional theory (DFT) calculations are provided in the ESI.

3. Results and discussion

3.1. Phase and microstructure of $\text{Fe}_2\text{O}_3/\text{ZnCo}_2\text{O}_4$

The formation process of the hexagonal star-shaped $\text{Fe}_2\text{O}_3/\text{ZnCo}_2\text{O}_4$ is shown in Scheme 1. The interpenetrating twin $\text{Zn}_1\text{Co}_{0.5}$ -ZIF precursors are first constructed through the addition of surfactants and adjustment of the Zn/Co ratio. Subsequently, $\text{Fe}^{\delta+}$ is introduced into the crystal using an ion-exchange method, during which the amount of $\text{Fe}^{\delta+}$ is controlled by the reaction time. Finally, a biphasic composite catalytic material $\text{Fe}_2\text{O}_3/\text{ZnCo}_2\text{O}_4$ is prepared via one-step calcination and oxidation to enhance the oxygen evolution reaction (OER) performance.

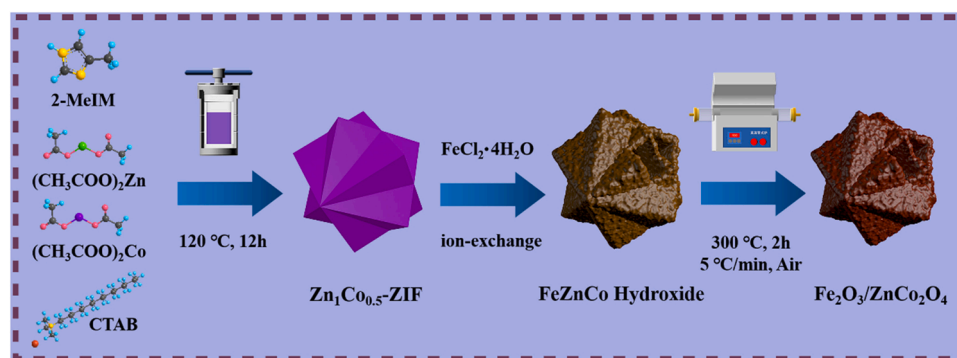
The morphology of $\text{Fe}_2\text{O}_3/\text{ZnCo}_2\text{O}_4$ is investigated using SEM and TEM. As shown in the SEM images in Fig. 1(a), interpenetrating twin $\text{Zn}_1\text{Co}_{0.5}$ -ZIF precursors with uniform sizes and smooth surfaces are successfully prepared. We also adjust the Zn/Co ratio to prepare a series of Zn_xCo_y -ZIF precursors (Fig. S1). With an increase in the amount of $\text{Co}^{\delta+}$, the shape of the hexagons gradually decreases, and flakes and cubes of different sizes appear. The final determination of the $\text{Co}^{\delta+}$ amount is 0.5 mmol, which is found to maintain the optimal morphology. Subsequently, $\text{Zn}_1\text{Co}_{0.5}$ -ZIF is exchanged with $\text{Fe}^{\delta+}$ to obtain FeZnCo Hydroxide (Fig. 1c). The shape of the material remains almost the same, but the surface becomes rougher. This is due to the tendency of the surface to form double-layer metal hydroxides (LDH) analogs during ion exchange [23,24]. A series of FeZnCo Hydroxide-X is obtained by controlling the ion exchange time (Fig. S2). Eventually, the LDH analogs on the surface gradually become thicker than the thin sheets. After performing ion exchange for 2 h, the structure appears to break, and obvious hollow structures are observed. Finally, $\text{Fe}_2\text{O}_3/\text{ZnCo}_2\text{O}_4$ is obtained via one-step calcination and oxidation as shown in Fig. 1(e). The hexagonal star-shaped structure is maintained, and a small number of pores appear, which is conducive to increasing the specific surface area [25].

The TEM images provide a clearer view of the internal structure of the material. TEM image in Fig. 1(b) clearly shows that $\text{Zn}_1\text{Co}_{0.5}$ -ZIF is a solid hexagonal star form of two interspersed cubes. In Fig. S5(d) it can be seen that $\text{Zn}_1\text{Co}_{0.5}$ -ZIF is calcined and oxidized to yield ZnCo_2O_4 . Its internal structure is still solid, but porous thin crystals appear on its surface. This shows that calcined oxidation is beneficial for increasing the specific surface area and improving the porosity [6]. FeZnCo Hydroxide is obtained by $\text{Fe}^{\delta+}$ exchange as shown in Fig. 1(d), and a thicker shell is observed on its surface, which is considered an LDH analog. This result is consistent with the SEM results. Apparent hollow nanostructures can be observed inside, and their formation can be attributed to dissolution and precipitation mechanisms [11]. Protons generate by the hydrolysis of FeCl_2 gradually corrode the ZIF precursor. Meanwhile, Zn^{2+} , $\text{Co}^{\delta+}$, and $\text{Fe}^{\delta+}$ are uniformly co-precipitated on the surface to

form FeZnCo hydroxide via methanol hydrolysis. Notably, methanol plays an important role in balancing the relative rates between dissolution and precipitation processes, thereby preventing the collapse of structure and separate precipitation [26]. As shown in Fig. S6, the FeZnCo hydroxide shell forms preferentially over hollow core during the ion-exchange process. It is shown that the etching of ZIF precursors occurs later than the co-deposition. The structure of the $\text{Fe}_2\text{O}_3/\text{ZnCo}_2\text{O}_4$ obtained by calcination and oxidation, as shown in Fig. 1(f), is maintained, and the near-transparent shells are thin. Thin shells not only accelerate mass transfer but also enhance the exposure of active sites, thus improving the electrocatalytic performance [27]. The elemental mapping (Fig. 1g) shows that Fe, Zn, Co, and O are uniformly distributed on the upper hexagonal star.

The HRTEM image in Fig. 2(b) shows three distinctly different lattice stripes with lattice spacing of 1.70 Å, 2.71 Å, and 2.34 Å, respectively. Those correspond to the (116) and (104) crystal planes of Fe_2O_3 and (222) crystal planes of ZnCo_2O_4 , respectively. The lattice spacing is slightly larger than that of the standard card owing to the lattice strain resulting from the interaction between Fe_2O_3 and ZnCo_2O_4 [28]. An obvious heterojunction is observed between the internal ZnCo_2O_4 and the outer shell Fe_2O_3 , which is favorable for electron transfer. The lattice striations are blurred and discontinuous, indicating the low crystallinity of $\text{Fe}_2\text{O}_3/\text{ZnCo}_2\text{O}_4$ [29]. Selected area electron diffraction patterns show the crystallographic characteristics of single and polycrystalline coexistence of $\text{Fe}_2\text{O}_3/\text{ZnCo}_2\text{O}_4$ (Fig. 2c and d). Fig. 2(c) diffraction array corresponding to the ZnCo_2O_4 , which shows isotropic regular crystalline dots, indicating ZnCo_2O_4 is a single crystal. Single crystals help maintain the integrity of the internal structural morphology and inhibit the dissolution of transition metals [30], which in turn reduces the occurrence of side reactions between the electrode and electrolyte. Fig. 2(d) shows the diffraction of the Fe_2O_3 shell, and the diffraction rings correspond to the (104), (202), and (214) planes (JCPDS No. 01–086–0550). The weaker diffraction rings indicate a lack of regular periodicity in the atomic lattice and low crystallinity, which is consistent with the HRTEM results. The lower crystallinity suggests the presence of defects in the structure, which can provide more active sites during the OER and facilitate the OER [31].

Fig. 3(a) shows the XRD spectra of $\text{Fe}_2\text{O}_3/\text{ZnCo}_2\text{O}_4$, ZnCo_2O_4 and Fe_2O_3 . In $\text{Fe}_2\text{O}_3/\text{ZnCo}_2\text{O}_4$, the characteristic peaks at 31.2° , 36.8° , 44.8° , 59.3° , and 65.2° correspond to the (220), (311), (400), (511), and (440) crystal planes of ZnCo_2O_4 , respectively (JCPDS No. 00–023–1390). The characteristic peaks at 33.1° , 35.7° , 49.5° , 54.0° , 62.5° , and 64.1° are the (104), (110), (024), (116), (214), and (300) crystal planes of Fe_2O_3 , respectively (JCPDS No. 01–086–0550). This indicates that $\text{Fe}_2\text{O}_3/\text{ZnCo}_2\text{O}_4$ is successfully synthesized. In ZnCo_2O_4 , the characteristic peak of ZnCo_2O_4 is significantly enhanced compared to that of $\text{Fe}_2\text{O}_3/\text{ZnCo}_2\text{O}_4$, indicating a decrease in the material crystallinity after $\text{Fe}^{\delta+}$ exchange. The strong ZIF peak (Fig. S8), suggests incomplete calcination and oxidation. In Fe_2O_3 , only a broad peak, corresponding to the (012) crystal plane of Fe_2O_3 exists, which indicates



Scheme 1. Schematic illustration for the synthetic process of $\text{Fe}_2\text{O}_3/\text{ZnCo}_2\text{O}_4$.

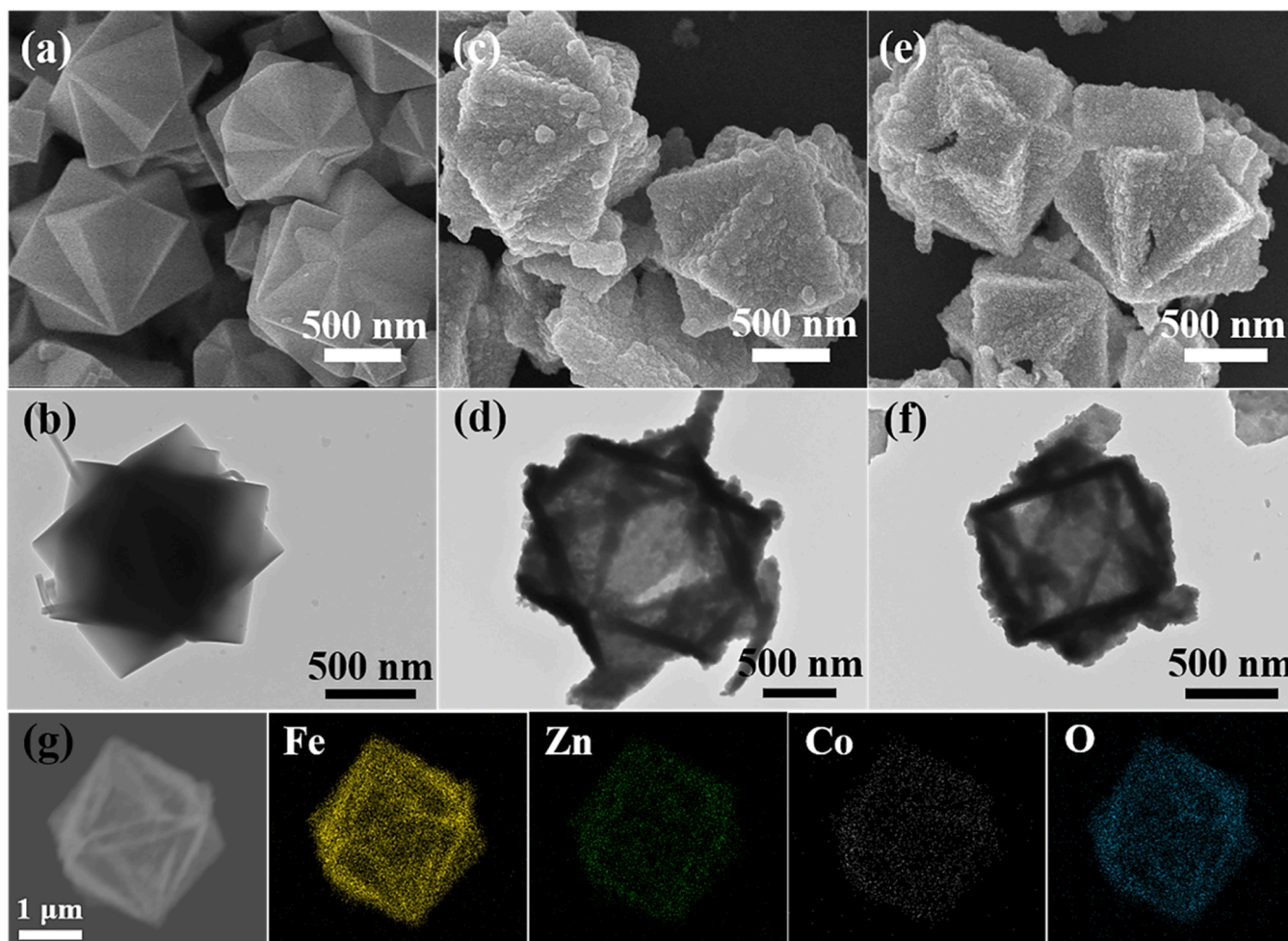


Fig. 1. SEM and TEM images of (a) and (b) $\text{Zn}_1\text{Co}_{0.5}\text{-ZIF}$; (c) and (d) FeZnCo Hydroxide; (e) and (f) $\text{Fe}_2\text{O}_3/\text{ZnCo}_2\text{O}_4$; (g) TEM-EDS mapping of the $\text{Fe}_2\text{O}_3/\text{ZnCo}_2\text{O}_4$ composite.

its poor crystallinity. The structure of $\text{Fe}_2\text{O}_3/\text{ZnCo}_2\text{O}_4$ is further confirmed by the Raman spectrum shown in Fig. 3(b). Three strong peaks at 212, 272, and 381 cm^{-1} correspond to the A_{1g} and E_g mode of $\alpha\text{-Fe}_2\text{O}_3$ [32], and another peak at around 699 cm^{-1} is assigned to the A_{1g} mode of ZnCo_2O_4 [33]. In comparison with pure Fe_2O_3 , it is found that all stretching vibrational bands of $\alpha\text{-Fe}_2\text{O}_3$ are shifted toward the lower energy band. A comparison with ZnCo_2O_4 reveals that its A_{1g} symmetric stretching band shifts toward a higher energy band. This suggests that electron transfer occurs between Fe_2O_3 and ZnCo_2O_4 , which is beneficial for improving the OER reaction activity [31]. From the plots of N_2 adsorption-desorption isotherms and pore size distribution (Fig. S9), the large specific surface area provided by the porous skeleton of ZnCo_2O_4 decrease after $\text{Fe}^{\delta+}$ exchange. Specific values are listed in Table S2. The specific surface area of $\text{Fe}_2\text{O}_3/\text{ZnCo}_2\text{O}_4$ is determined to be $67.9\text{ m}^2\text{ g}^{-1}$ and its mesoporous structure can be seen through pore size analysis with an average pore size of 3.4 nm. The high specific surface area and mesoporous structure provide a rich active area between the electrode and electrolyte, thereby facilitating electron migration [34].

The elemental compositions and valence states of the surfaces are further explored. $\text{Fe}_2\text{O}_3/\text{ZnCo}_2\text{O}_4$, ZnCo_2O_4 , and Fe_2O_3 are characterized by XPS. As shown in Fig. S10, the XPS spectrum of $\text{Fe}_2\text{O}_3/\text{ZnCo}_2\text{O}_4$ clearly shows six peaks corresponding to Zn, Fe, O, N, Co, and C. A clear Co peak is observed for ZnCo_2O_4 , but not for $\text{Fe}_2\text{O}_3/\text{ZnCo}_2\text{O}_4$. In addition, the peak intensities of Zn and N weakened. This may be attributed to the surface being covered with excess Fe_2O_3 ; thus, the signal of each element in the backbone is weakened. Also, the amount of Co is less and

more difficult to detect [11]. As displayed in Fig. 3(c), the high-resolution spectrum of Fe 2p includes six peaks with binding energies at 710.6 eV and 723.9 eV caused by Fe $2p_{3/2}$ and Fe $2p_{1/2}$ of Fe^{3+} in Fe_2O_3 . The peaks at 713.5 eV and 727.2 eV are associated with Fe $2p_{3/2}$ and Fe $2p_{1/2}$ of Fe^{2+} . The other two fit peaks at 718.5 eV and 732.2 eV are satellite peaks [23]. The peak area ratio of $\text{Fe}^{3+}/\text{Fe}^{2+}$ in $\text{Fe}_2\text{O}_3/\text{ZnCo}_2\text{O}_4$ change from 1.96 to 1.91 compare to pure Fe_2O_3 , indicating a decrease in the Fe^{3+} content. As shown in Fig. 3(d), the high-resolution spectrum of Zn 2p is fitted to two Zn^{2+} peaks located at binding energies of 1022.1 eV and 1045.0 eV, corresponding to Zn $2p_{3/2}$ and Zn $2p_{1/2}$, respectively. The Fe 2p orbital binding energy of the duplex $\text{Fe}_2\text{O}_3/\text{ZnCo}_2\text{O}_4$ is blue-shifted (-0.22 eV) compare to that of single-phase Fe_2O_3 , indicating electrons gains. The Zn 2p orbital binding energy is red-shifted ($+0.31\text{ eV}$), indicating loss of electrons. This confirms the existence of a strong electronic interaction between Fe_2O_3 and ZnCo_2O_4 . The interfacial electrons migrate from ZnCo_2O_4 to the surface of Fe_2O_3 , which increases the electron density on the surface of Fe_2O_3 and induces the reduction of Fe^{3+} [31]. The high-resolution spectra of C 1s are presented in Fig. 3(e), which shows three fitting peaks at 284.8, 286.6, and 288.5 eV. This corresponds to C-C, C-O, and O-C=O, which is consistent with previous literature [34]. As seen in Fig. 3(f) the high-resolution spectrum of O 1s can be fitted to three major peaks at 530.1, 531.6, and 533.4 eV, corresponding to lattice oxygen (O_L), surface active oxygen vacancies (O_V), and surface adsorbed oxygen (O_C) [17]. By analyzing the peak area ratio, it is evident that the $\text{Fe}_2\text{O}_3/\text{ZnCo}_2\text{O}_4$ composite has an O_L content of 60.7% and an O_V content of 34.5%, indicating a lower concentration of lattice oxygen and a higher

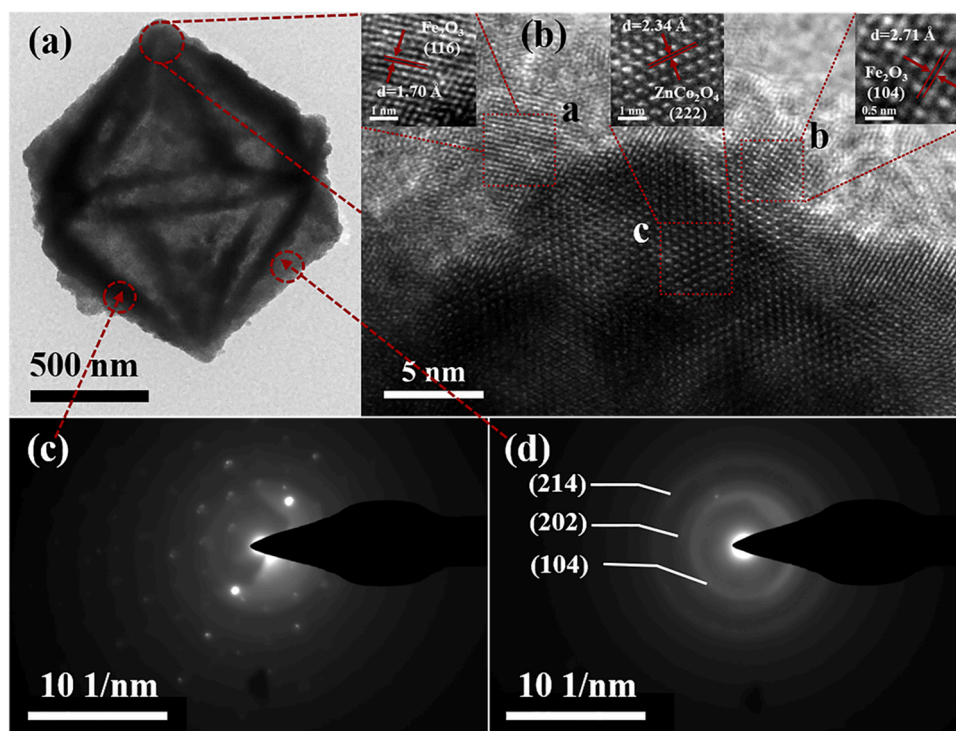


Fig. 2. (a and b) TEM and HRTEM images of the $\text{Fe}_2\text{O}_3/\text{ZnCo}_2\text{O}_4$ composite; Selected area electron diffraction pattern of (c) ZnCo_2O_4 framework; (d) Fe_2O_3 shell.

concentration of O_V compare to Fe_2O_3 and ZnCo_2O_4 (Table S2). Combine with the EPR test results (Fig. S11), the intensity of the O_V peak at $g = 2.003$ is stronger for $\text{Fe}_2\text{O}_3/\text{ZnCo}_2\text{O}_4$ than for ZnCo_2O_4 . There are no O_V in Fe_2O_3 . This suggests that the O_V content increases after $\text{Fe}^{\delta+}$ exchange, which is consistent with the XPS results [17]. This is caused by the different binding energies of Fe and Zn/Co atoms for O. $\text{Fe}^{\delta+}$ doping changes the charge density distribution around the O atom, causing the O atom to detach from the surface and thus forming O_V [35]. In addition, the escape O atoms increase the energy state of the adjacent metal cations, which facilitates their adsorption of OH^- , resulting in an effective improvement in the efficiency of the OER reaction [36].

3.2. Electrochemical performances and mechanism analysis of OER

To clarify the role of $\text{Fe}^{\delta+}$ introduction and explore the optimal amount of $\text{Co}^{\delta+}$ and $\text{Fe}^{\delta+}$. The OER activities of $\text{Fe}_2\text{O}_3/\text{ZnCo}_2\text{O}_4$, ZnCo_2O_4 , Fe_2O_3 , and RuO_2 are evaluated in 1.0 M KOH and corrected by i_R (90%). The LSV curves are shown in Fig. 4(a), Figs. S12 and S13. It is observed that the bare ZnCo_2O_4 shows trivial OER activity, while the elaborate $\text{Fe}_2\text{O}_3/\text{ZnCo}_2\text{O}_4$ shows the highest current density at the same potential. To achieve a current density of 10 mA cm^{-2} , $\text{Fe}_2\text{O}_3/\text{ZnCo}_2\text{O}_4$ needs an overpotential of 261 mV, which is lower than those of Fe_2O_3 (289 mV), RuO_2 (337 mV) and ZnCo_2O_4 (359 mV) (Fig. 4b). With increasing amounts of $\text{Co}^{\delta+}$ and $\text{Fe}^{\delta+}$, the OER activity first increased and then decreased (Figs. S12 and S13). Finally, 0.5 mmol of $\text{Co}^{\delta+}$ and 1 h of $\text{Fe}^{\delta+}$ exchanging is determined as the optimal synthesis conditions. The Tafel slopes of the catalysts are examined to determine their OER kinetics. The Tafel slope of 71.8 mV dec^{-1} for $\text{Fe}_2\text{O}_3/\text{ZnCo}_2\text{O}_4$ as shown in Fig. 4(c) is lower than that of Fe_2O_3 (72.0 mV dec^{-1}), RuO_2 ($154.2 \text{ mV dec}^{-1}$) and ZnCo_2O_4 ($105.5 \text{ mV dec}^{-1}$), indicating high intrinsic electrocatalytic activity. To further understand the intrinsic activity of these catalysts, CV is used to measure different scan rates (20, 40, 60, 80, and 100 mV s^{-1}) in the non-Faraday region (Figs. S14–16). As shown in Fig. 4(d), the C_dl value of 2.8 mF cm^{-2} for $\text{Fe}_2\text{O}_3/\text{ZnCo}_2\text{O}_4$ is higher than that of 2.3, 1.2, and, 1.3 mF cm^{-2} for Fe_2O_3 , RuO_2 , and ZnCo_2O_4 , respectively. The C_dl results indicate that $\text{Fe}_2\text{O}_3/\text{ZnCo}_2\text{O}_4$ has

strong electrocatalytic active sites. Subsequently, the electrochemical active area (ECSA) of these electrocatalysts is obtained using C_dl values according to available reports [27]. As illustrate in Fig. 4(e), the ECSA of $\text{Fe}_2\text{O}_3/\text{ZnCo}_2\text{O}_4$, Fe_2O_3 , RuO_2 , and ZnCo_2O_4 are 70, 57.5, 30, and 32.5 cm^2 , respectively. The geometric current density is further normalized using the ECSA to compare the intrinsic activities of the various catalysts. Expectedly, $\text{Fe}_2\text{O}_3/\text{ZnCo}_2\text{O}_4$ exhibits the highest catalytic performance (Fig. 4f), indicating its excellent intrinsic activity.

EIS is an efficient way to understand the kinetic processes of electrochemical reactions, specifically to study the kinetics of reactants' adsorption and desorption on the electrode surface [22]. Fig. 5(a) depicts the Nyquist plots of $\text{Fe}_2\text{O}_3/\text{ZnCo}_2\text{O}_4$, ZnCo_2O_4 , RuO_2 , and Fe_2O_3 at 300 mV overpotential, reflecting their different electrochemical reaction behaviors. An equivalent circuit is used to fit the data, and the best-fit parameters are listed in Table S4. The charge transfer resistance (R_ct) of $\text{Fe}_2\text{O}_3/\text{ZnCo}_2\text{O}_4$ is 0.82Ω smaller than that of Fe_2O_3 (1.43Ω), RuO_2 (11.05Ω) and, ZnCo_2O_4 (16.73Ω), which indicate that fast charge transfer kinetics occur at the $\text{Fe}_2\text{O}_3/\text{ZnCo}_2\text{O}_4$ electrolyte interface, resulting in good OER kinetics [17]. The high-frequency region (HF) is related to the oxidation inside the electrode, and the low-frequency region (LF) is concerned with the charge inhomogeneity caused by the oxidized material present at the electrode interface [22]. As shown in Fig. 5(b), when the applied potential exceeds 1.12 V vs. RHE, the phase angle in the HF region becomes significantly smaller and exhibits electrocatalytic oxidation. Above 1.35 V vs. RHE, the phase angle of the LF region decreases significantly for the OER to occur [22,37]. From Fig. 5 (b-d) and Fig. S17, it can be seen that the electrooxidation rate and OER reaction process of $\text{Fe}_2\text{O}_3/\text{ZnCo}_2\text{O}_4$ are both faster than the other catalysts. These results suggest that the distinctive hexagonal hollow structure, in which $\text{Fe}_2\text{O}_3/\text{ZnCo}_2\text{O}_4$ has a large surface area and abundant mesopores, effectively promotes charge and mass transfer, leading to improved OER performance.

Various chronopotentiometric curves acquire on $\text{Fe}_2\text{O}_3/\text{ZnCo}_2\text{O}_4$ (Fig. 6a) show beneficial mass transport properties (adsorption of OH^- and separation of oxygen bubbles), in addition to demonstrating good electrical conductivity [18]. Stability is the other critical parameter to

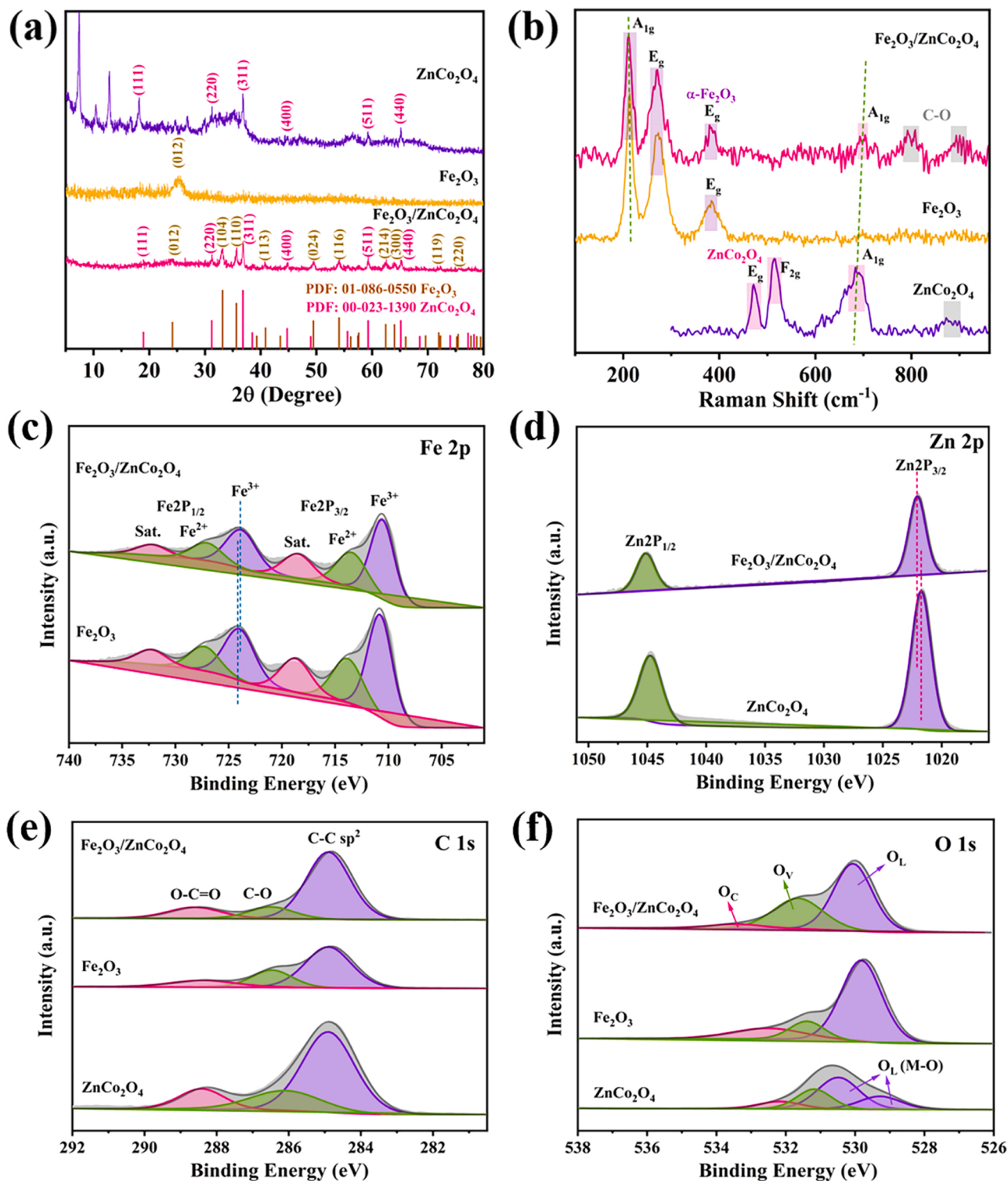


Fig. 3. (a) XRD patterns; (b) Raman spectra; the high-resolution X-ray photoelectron spectrum of $\text{Fe}_2\text{O}_3/\text{ZnCo}_2\text{O}_4$, ZnCo_2O_4 and Fe_2O_3 (c) Fe 2p, (d) Zn 2p, (e) C 1s, (f) O 1s.

evaluate the performance of electrocatalysts [11,38]. To investigate the OER stability of $\text{Fe}_2\text{O}_3/\text{ZnCo}_2\text{O}_4$, the LSV curves before and after 1000 consecutive CVs are recorded, and the initial and final curves almost overlapped in the OER region (inset of Fig. 6b). From the long-term chronoamperometry curve in Fig. 6(b), it can be seen that the OER potential is maintained at 98.0% and 98.8% for 50 h at current densities of 20 and 50 mA cm^{-2} , respectively. These results confirm the excellent stability and robustness of $\text{Fe}_2\text{O}_3/\text{ZnCo}_2\text{O}_4$ for the OER. The turnover

frequency (TOF) define as the number of O_2 molecules produces by each active site per second refers to the intrinsic activity of the catalyst [22, 39]. The TOF value of $\text{Fe}_2\text{O}_3/\text{ZnCo}_2\text{O}_4$ at $\eta = 300 \text{ mV}$ (0.053 s^{-1}) is also significantly better than those of the ZnCo_2O_4 (0.012 s^{-1}) and Fe_2O_3 (0.017 s^{-1}), and so on (Fig. 6c and S18). These results demonstrate that $\text{Fe}_2\text{O}_3/\text{ZnCo}_2\text{O}_4$ is an efficient OER catalyst. The OER performance of the Co-Fe-based catalysts reported in recent articles is summarized in Fig. 6 (d) and Table 1. Hollow hexagonal $\text{Fe}_2\text{O}_3/\text{ZnCo}_2\text{O}_4$ has a much better

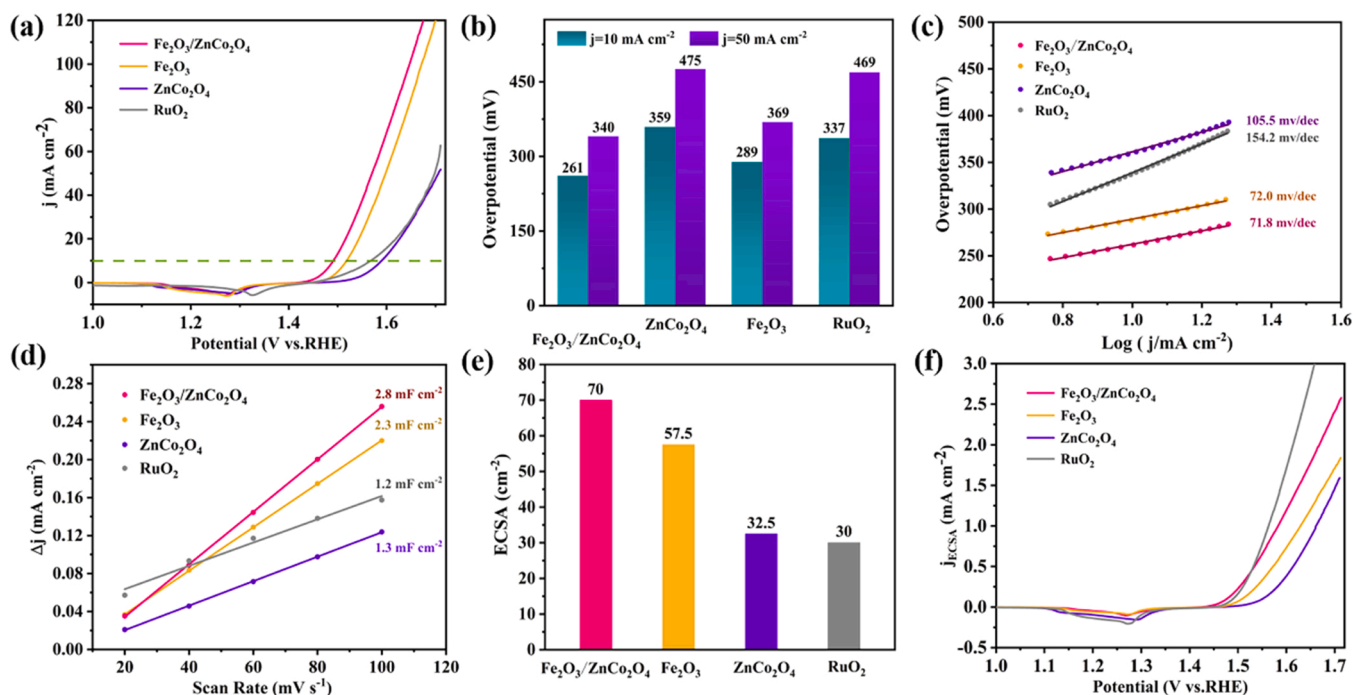


Fig. 4. Electrochemical performance of $\text{Fe}_2\text{O}_3/\text{ZnCo}_2\text{O}_4$, ZnCo_2O_4 , Fe_2O_3 and RuO_2 . (a) LSV curves at a scan rate of 5 mV s^{-1} ; (b) the overpotentials at 10 and 50 mA cm^{-2} ; (c) Tafel plots; (d) the C_{dl} ; (e) ECSA evaluation; (f) LSV curves normalized by the ECSA.

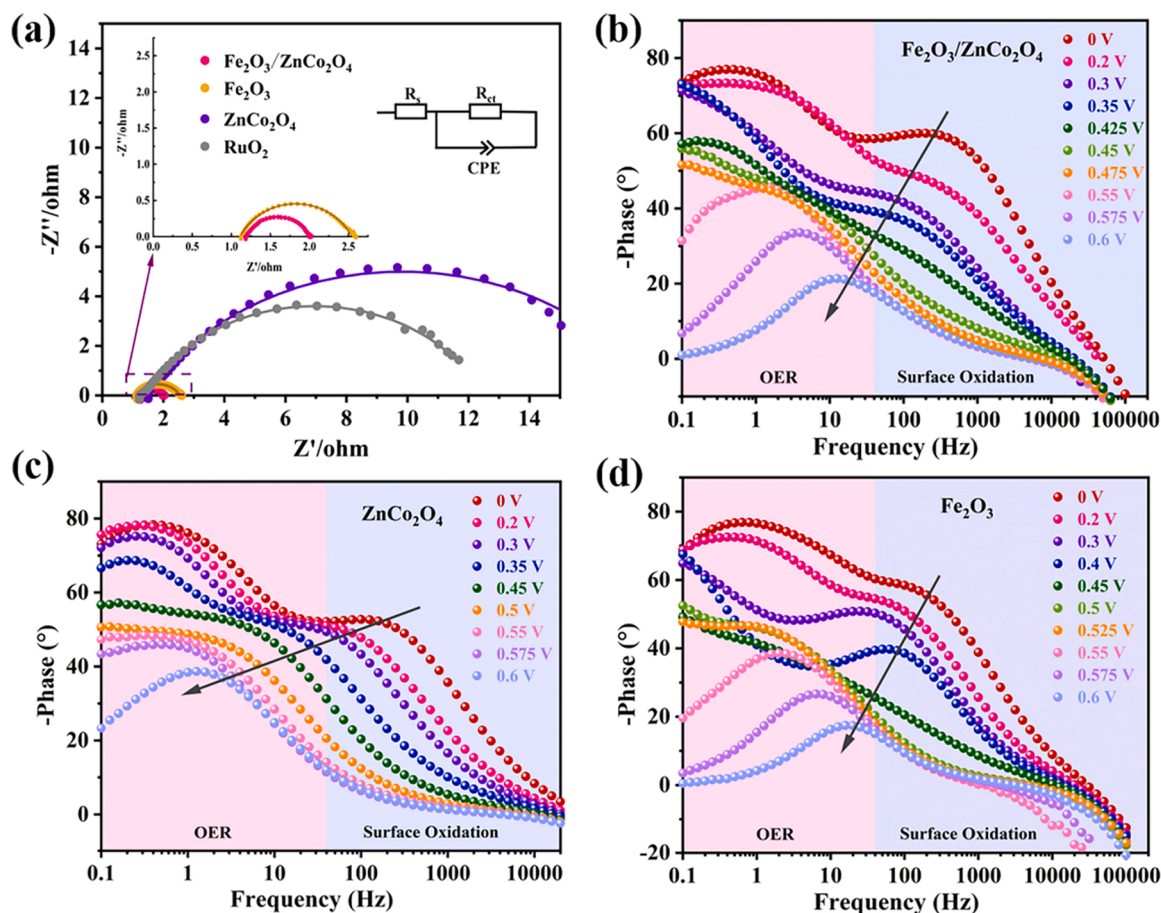


Fig. 5. (a) Nyquist plots of $\text{Fe}_2\text{O}_3/\text{ZnCo}_2\text{O}_4$, ZnCo_2O_4 , Fe_2O_3 and RuO_2 ; Bode-phase plots of (b) $\text{Fe}_2\text{O}_3/\text{ZnCo}_2\text{O}_4$; (c) ZnCo_2O_4 ; (d) Fe_2O_3 .

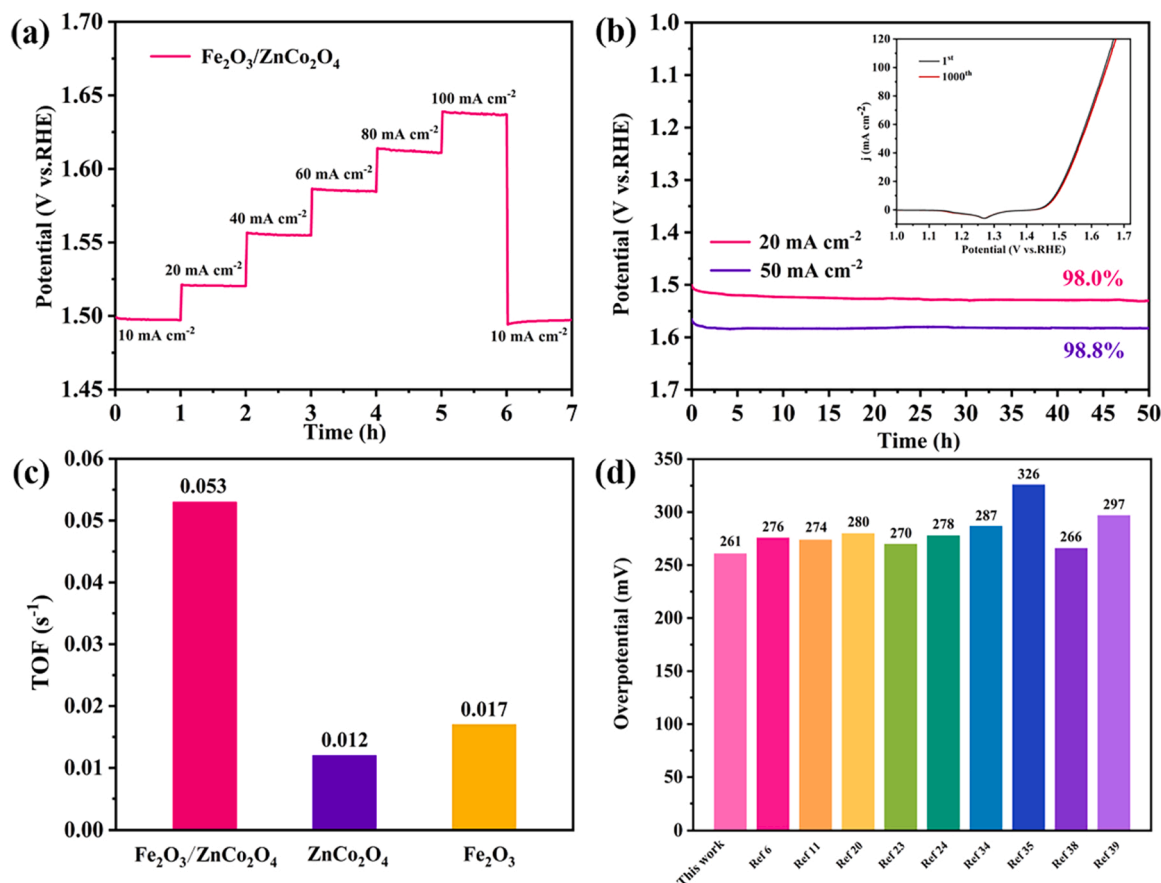


Fig. 6. (a) Rate performance of Fe₂O₃/ZnCo₂O₄ at various current densities; (b) Long-time chronoamperometry of Fe₂O₃/ZnCo₂O₄ at 20 mA cm⁻² and 50 mA cm⁻² for 50 h (inset: LSV for initial and after 1000 cycles CV); (c) TOF and mass activity results; (d) Comparison of OER performances for Fe₂O₃/ZnCo₂O₄ with previously reported electrocatalysts.

Table 1

List of some recent work on Co-Fe-based catalysts for oxygen evolution reaction.

Materials	Current density (mA cm ⁻²)	Overpotential (mV)	Durability (h)	Refs.
Co(CO ₃) _{0.5} OH@CC nanoneedle	10	276	25	[6]
CoFe _x -O hollow nanocages	10	274	30	[11]
UCoO ₄ /Co ₃ O ₄ Heterojunction	10	280	20	[20]
Co-Fe LDHs nanosheet	10	270	12	[23]
NiCoFe-HO@NiCo-LDH yolk-shelled microrods	10	278	11	[24]
CoO@Co ₃ O ₄ /C nanocomposites	10	287	30	[34]
CoFe ₂ O ₄ single-phase	10	326	10	[35]
CoP ₂ /Fe-CoP ₂ yolk-shell nanoboxes	10	266	10	[38]
Co ₃ O ₄ /Co-Fe oxide double-shell nanoboxes	10	297	10	[39]
Fe ₂ O ₃ /ZnCo ₂ O ₄ hexagonal star interpenetration twin	10	261	35	This work

OER performance than other recently reported OER electrocatalysts. These results indicate that Fe₂O₃/ZnCo₂O₄ with a hollow structure and abundant active sites is a favorable OER catalyst under alkaline conditions.

To further understand the stability of the Fe₂O₃/ZnCo₂O₄ structure,

Fe₂O₃/ZnCo₂O₄ is characterized using SEM, TEM, Raman, and XPS after stability testing. The SEM and TEM images (Fig. 7a and b) show that Fe₂O₃/ZnCo₂O₄ maintains a hexagonal star-shaped morphology after the OER. No structure collapse occurs, confirming the stability of Fe₂O₃/ZnCo₂O₄. As observe in the Raman spectrum (Fig. 7c), the overall peak intensity increases after the OER, indicating the activation of Fe₂O₃/ZnCo₂O₄. One peak at 585.1 cm⁻¹ appears, corresponding to the symmetric stretching A_{1g} of O-Co-O [40]. This implies that the generation of metal hydroxides, which are usually considered as active sites, is more favorable for the OER [27]. Moreover, XPS measurements are conducted to investigate the surface chemical states of Fe₂O₃/ZnCo₂O₄ after the OER test. As shown in Fig. 7(d), no significant change is observed in the elemental species before and after the reaction. After the OER reaction, in the high-resolution C 1 s spectrum (Fig. 7e), a satellite peak at 292.2 eV is observed, owing to the π -electron leap [41]. In the O 1 s spectrum, a decrease in O_L and an increase in O_V and O_C can be observed (Fig. 7f and Table S3). This may be attributed to the increase in defects caused by surface reconstruction during the OER, and the increase in O_V may be a critical factor in increasing the activity of Fe₂O₃/ZnCo₂O₄ [22, 41].

The electron transfer at the Fe₂O₃/ZnCo₂O₄ heterojunction interface is further explored. The energy band structure is examined using UV-vis spectroscopy (Fig. S19), Mott-Schottky (MS) plots and valence band spectra. The absorption direct transition bandgap energy, E_g , is determined using the following equation [42]:

$$(ah\nu)^n = K(h\nu - E_g)$$

where $h\nu$ is the photo energy, α is the absorption coefficient, K is a constant relative to the material. The Tauc curves of Fe₂O₃/ZnCo₂O₄,

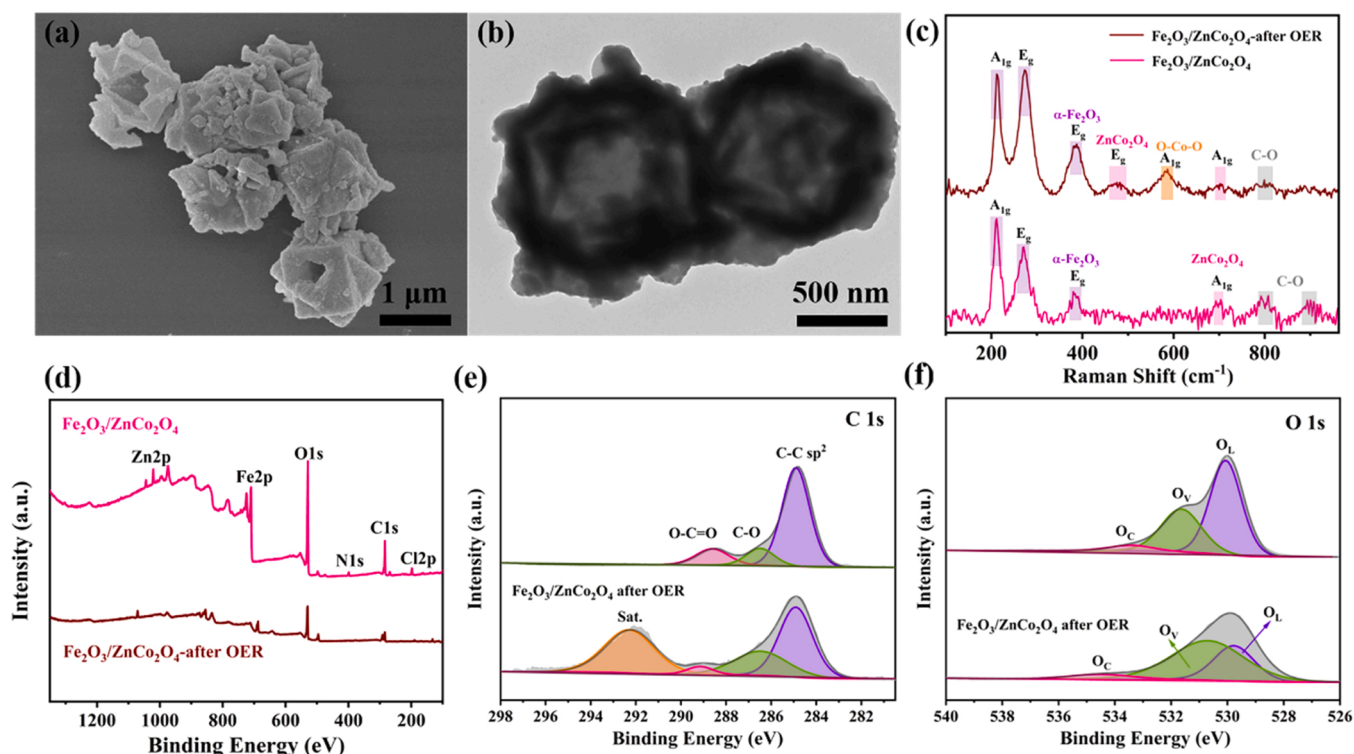


Fig. 7. Structure characterizations of $\text{Fe}_2\text{O}_3/\text{ZnCo}_2\text{O}_4$ initial and after stability test (a) SEM images after OER; (b) TEM images after OER; (c) Raman spectra; (d) the survey spectrum; the high-resolution XPS spectra of (e) C1s; (f) O1s.

Fe_2O_3 , and ZnCo_2O_4 are shown in Fig. 8(a). The bandgap energies of $\text{Fe}_2\text{O}_3/\text{ZnCo}_2\text{O}_4$, Fe_2O_3 , and ZnCo_2O_4 are calculated as 1.72, 1.80, and 1.87 eV, respectively. The bandgap of the biphasic composite $\text{Fe}_2\text{O}_3/\text{ZnCo}_2\text{O}_4$ is smaller than those of pure Fe_2O_3 and ZnCo_2O_4 . This implies a faster electron mobility, which facilitates catalytic reactions [33].

As shown in the MS plots of Fig. 8(b-c), Fe_2O_3 and ZnCo_2O_4 exhibit a positive slope, indicating that they are n-type semiconductors [43]. Intersecting the tangent line of the slope with the transverse coordinate, we obtain the Fe_2O_3 and ZnCo_2O_4 flat band potentials of -0.42 V and -0.55 V, respectively (vs. Ag/AgCl). Generally, the flat band potential is 0.3 V positive over the bottom of the conduction band potential (E_{CB}) for n-type semiconductors [44]. Combining the energy band gap and E_{CB} positions, the energy band structures of Fe_2O_3 and ZnCo_2O_4 are schematically shown in Fig. 8(d) (based on $E_{\text{g}} = E_{\text{CB}} - E_{\text{VB}}$). In addition, the valence band spectrum (Fig. S19) is obtained near the Fermi energy level (E_{F}) using XPS, and it is possible to determine the position of the E_{F} relative to the valence band maximum (V_{BM}) [45]. The E_{F} values of Fe_2O_3 and ZnCo_2O_4 are higher than V_{BM} 0.68 V and 0.45 V, respectively. When Fe_2O_3 and ZnCo_2O_4 form a heterojunction interface, electrons automatically flow from the conduction band of ZnCo_2O_4 with a high E_{F} to that of Fe_2O_3 with a low E_{F} , causing charge transfer and energy band bending (Fig. 8e) [22].

The results mentioned above, in combination with the HRTEM image of $\text{Fe}_2\text{O}_3/\text{ZnCo}_2\text{O}_4$ shown in Fig. 2(b), provide evidence for the formation of $\text{Fe}_2\text{O}_3/\text{ZnCo}_2\text{O}_4$ (n-n) heterojunction. The presence of the n-n heterojunction between Fe_2O_3 and ZnCo_2O_4 creates a built-in electric field that facilitates electron transport [46]. This results in the formation of a positive charge center on the Fe_2O_3 surface, which is favorable for electron transfer from OH^- to Fe_2O_3 [11]. The electrons will then recombine with the holes in the valence band of Fe_2O_3 . The $\text{Fe}_2\text{O}_3/\text{ZnCo}_2\text{O}_4$ interface with the n-n heterojunction can accelerate electron transport and effectively optimize the surface electronic state. Therefore, the $\text{Fe}_2\text{O}_3/\text{ZnCo}_2\text{O}_4$ material exhibits high electrocatalytic activity.

DFT calculations are performed to further elucidate the mechanism underlying the enhanced OER catalytic activity by forming an n-n

heterojunction with the O_{V} . The (111) facet of ZnCo_2O_4 and the (001) facet of Fe_2O_3 are selected as models because these two facets have a high degree of lattice matching. Based on the EPR results, an O_{V} concentration of 1.56% is introduced in the modeling process. Fig. 9(a) shows the optimized catalyst models (other views of the models are shown in Fig. S20). The density of states (DOS) of $\text{Fe}_2\text{O}_3/\text{ZnCo}_2\text{O}_4$, Fe_2O_3 , and ZnCo_2O_4 are calculated to provide deeper insight into the role of heterojunction in the OER. As shown in Fig. 9(b), the DOS of $\text{Fe}_2\text{O}_3/\text{ZnCo}_2\text{O}_4$, Fe_2O_3 , and ZnCo_2O_4 are all continuous near the Fermi energy level, indicating that they all exhibit narrow band gaps and excellent conductivities [47]. The DOS intensity at the Fermi energy level suggests that the conductivity of pure ZnCo_2O_4 is poor, but the formation of heterojunction significantly enhances the conductivity of $\text{Fe}_2\text{O}_3/\text{ZnCo}_2\text{O}_4$, which is consistent with the EIS results. In $\text{Fe}_2\text{O}_3/\text{ZnCo}_2\text{O}_4$, the DOS near the Fermi energy level is primarily contributed by Fe and some Co, indicating that Fe and Co tend to be the main active sites in the OER reaction (Fig. 9b) [47]. In Fig. 9(c), it is found that the d-band centers (ε_{d}) of Fe, Co, and Zn shift toward the Fermi energy level after the formation of n-n heterojunction, which is due to the reconfiguration of the electronic states at the heterojunction interface, thereby reducing the occupation of antibonding orbital and optimization of the intrinsic activity of $\text{Fe}_2\text{O}_3/\text{ZnCo}_2\text{O}_4$ [6,48]. Moreover, the ε_{d} of Fe and Co is closer to the Fermi energy level and has stronger adsorption to the reaction intermediate state [49]. It is proved that the synergistic effect of heterojunction between Fe_2O_3 and ZnCo_2O_4 optimized the adsorption of the reaction intermediate and facilitated the continuation of the OER reaction.

The corresponding free-energy changes of the oxygen intermediates ($^*\text{O}$, $^*\text{OH}$, $^*\text{OOH}$, and O_2) are calculated to investigate the limiting reaction barriers (Fig. 9d and e). For $\text{Fe}_2\text{O}_3/\text{ZnCo}_2\text{O}_4$ and Fe_2O_3 , the formation of $^*\text{OOH}$ is the rate-determining step (RDS), and the highest barriers are 1.51 and 1.55 eV. However, the RDS for ZnCo_2O_4 is the last step to form O_2 ($\Delta G = 1.89$ eV). Additionally, at a potential of $U = 1.23$ V, the free-energy change profiles reveal the overpotential of the catalysts. The theoretical OER overpotentials of $\text{Fe}_2\text{O}_3/\text{ZnCo}_2\text{O}_4$, Fe_2O_3 ,

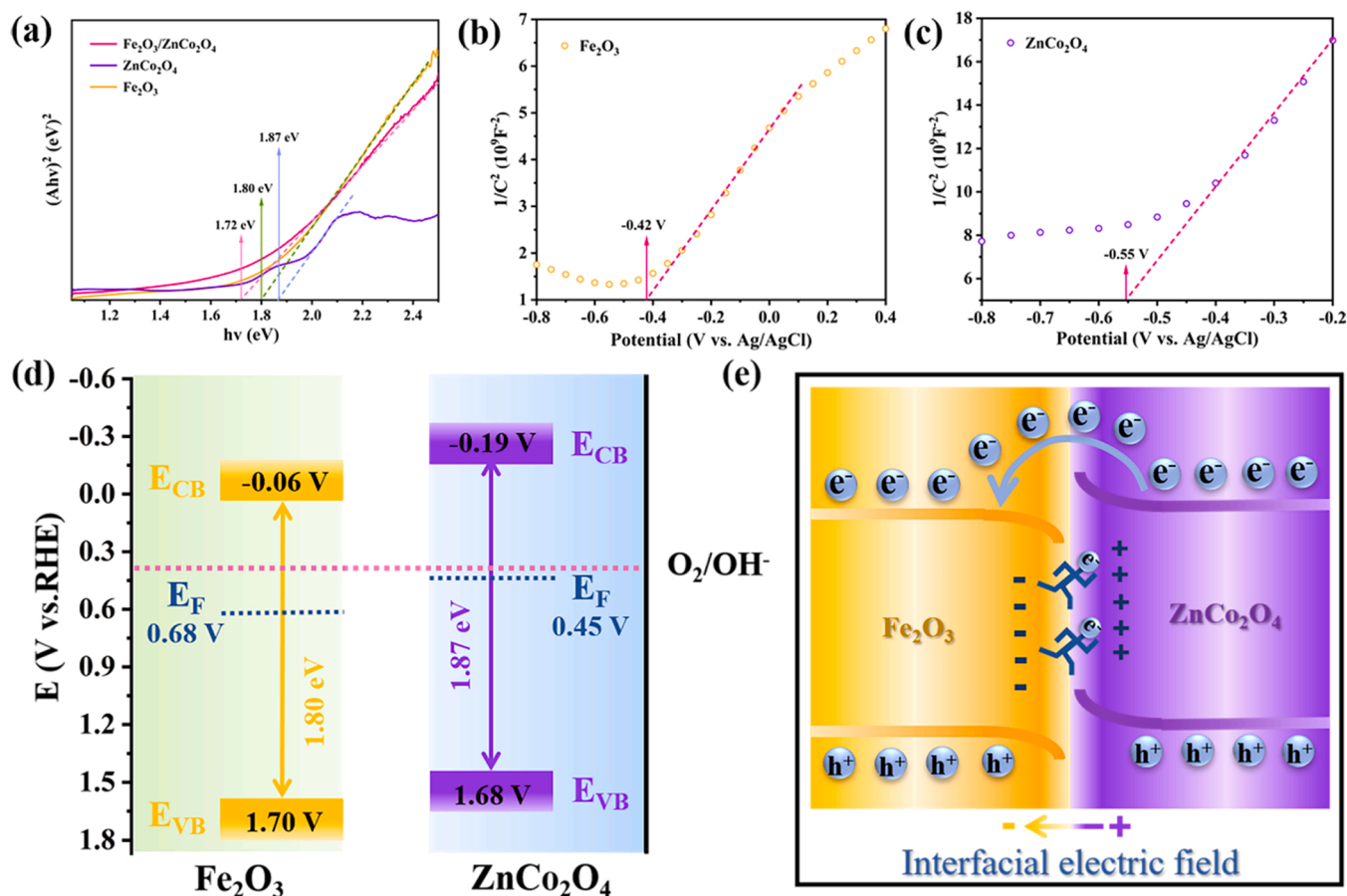


Fig. 8. (a) Band gap energy results of Fe₂O₃/ZnCo₂O₄, Fe₂O₃, and ZnCo₂O₄; (b) Mott-Schottky plots of Fe₂O₃; (c) Mott-Schottky plots of ZnCo₂O₄; (d) Energy band structure alignments of Fe₂O₃ and ZnCo₂O₄; (e) Schematic of interface electronic structure in the Fe₂O₃/ZnCo₂O₄ heterojunction.

and ZnCo₂O₄ are 281, 323, and 664 mV, respectively. These results are in agreement with the overpotentials measure in the experimental LSV curves. We also found that the adsorption energy of ZnCo₂O₄ for OH* is low, whereas that of Fe₂O₃ is high, and the adsorption energy of Fe₂O₃/ZnCo₂O₄ for OH* is intermediate. This is attributed to the heterojunction synergy between Fe₂O₃/ZnCo₂O₄ which adjusts the electronic state distribution of the central metal atoms and is the underlying reason for the higher OER activity exhibits by the catalyst [50]. The above results indicate that Fe₂O₃/ZnCo₂O₄ with n-n heterojunction and defects can effectively reduce the reaction energy barrier and accelerate the reaction kinetics compare with Fe₂O₃ and ZnCo₂O₄.

4. Conclusion

We create a highly effective catalyst for the evolution of alkaline oxygen by constructing a hexagonal hollow biphasic structure of Fe₂O₃/ZnCo₂O₄ with n-n heterojunction and defects. This results in a significantly higher OER activity compared to the pure phase. The reconstituted biphasic Fe₂O₃/ZnCo₂O₄ co-catalyst results in a 4.4-fold increase in the TOF of the OER compare to that of the single-phase catalyst (ZnCo₂O₄). An overpotential of only 261 mV is required to achieve a current density of 10 mA cm⁻², and the catalyst remains stable for 50 h under a large current density of 50 mA cm⁻². The exceptional OER performance can be attributed to the following characteristics. i) The unique hexagonal hollow structure increases the specific surface area of the material, allowing for faster diffusion of electrolytes and exposure to more active sites. ii) Phase separation due to Fe^{δ+} introduction, which reduces the crystallinity of the material, generates more O_v, and forms more active sites. iii) The construction of an n-n

heterojunction interface induces a spontaneous charge transfer and effectively optimizes the electronic state of the surface. The intrinsic activity of the active site is increased by improving the adsorption capacity of the Co and Fe centers for the oxygen-containing intermediates. The DFT results illustrate that the d-band center of each metal approaches the Fermi energy level after the construction of the Fe₂O₃/ZnCo₂O₄ heterostructure, which optimizes the adsorption and desorption of the intermediate state, thus significantly reducing the Gibbs free energy barrier of the decisive step of the OER and substantially enhancing the OER activity. This study uses a dual approach of direct characterization and DFT calculations to explore the intrinsic mechanism of OER performance enhancement at heterojunction interfaces, providing a new research insight for interface engineering construction. This discovery paves the way for the creation of novel and long-lasting catalysts for OER with exceptional performance.

CRediT authorship contribution statement

Sha-Qi Fu: Writing – original draft, Writing – review & editing, Conceptualization, Supervision, Project administration. **Yi-Ran Ma:** Writing – review & editing, Software, Supervision. **Xue-Chun Yang:** Writing – review & editing, Supervision. **Xuan Yao:** Software, Formal analysis. **Zheng Jiao:** Conceptualization, Funding acquisition, Supervision. **Ling-Li Cheng:** Writing – review & editing, Supervision. **Pan-Deng Zhao:** Conceptualization, Project administration, Supervision.

Declaration of Competing Interest

The authors declare that they have no known competing financial

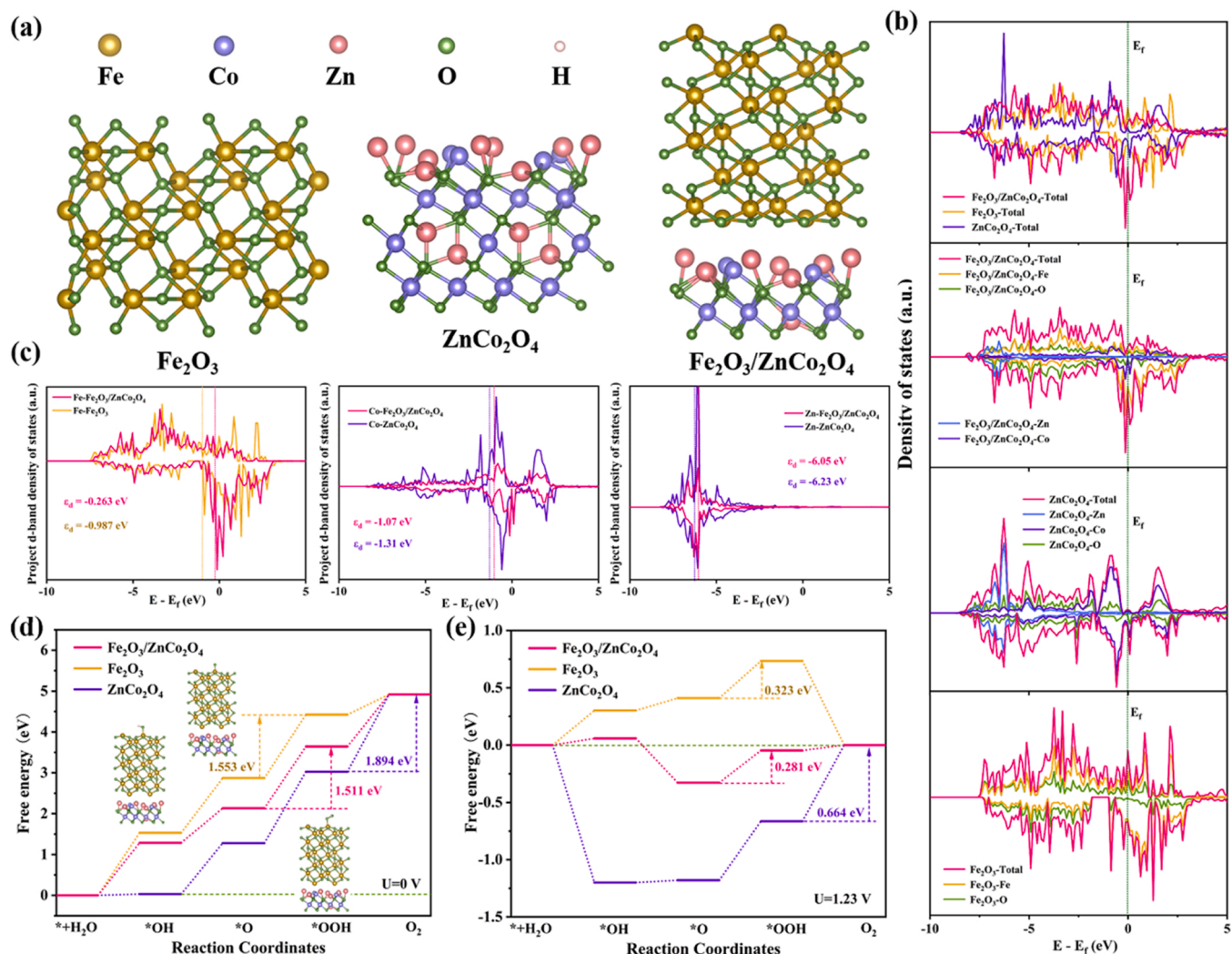


Fig. 9. (a) Optimized models of catalysts; (b) DOS of the catalysts; (c) d band center of Fe, Co, and Zn of the catalysts; (d) The energetic pathway of OER in the alkaline environment; (e) The energetic pathway of OER in the alkaline environment under the applied potential of 1.23 eV.

interests or personal relationships that could have appeared to influence the work reported in this paper.

Data Availability

No data was used for the research described in the article.

Acknowledgments

This work was supported by Shanghai Technical Service Center for Advanced Ceramics Structure Design and Precision Manufacturing (NO. 20DZ2294000). The Belt and Road Initiatives International Cooperation Project (NO. 20640770300). We also appreciate the High Performance Computing Center of Shanghai University, and Shanghai Engineering Research Center of Intelligent Computing System (No. 19DZ2252600) for providing computing resources and technical support.

Appendix A. Supporting information

Supplementary data associated with this article can be found in the online version at [doi:10.1016/j.apcatb.2023.122813](https://doi.org/10.1016/j.apcatb.2023.122813).

References

- [1] H. Song, J. Yu, Z. Tang, B. Yang, S. Lu, Halogen-doped carbon dots on amorphous cobalt phosphide as robust electrocatalysts for overall water splitting, *Adv. Energy Mater.* 12 (2022) 2102573.
- [2] X. Xie, J. Liu, C. Gu, J. Li, Y. Zhao, C. Liu, Hierarchical structured CoP nanosheets/carbon nanofibers bifunctional electrocatalyst for high-efficient overall water splitting, *J. Energy Chem.* 64 (2022) 503–510.
- [3] X. Chang, B. Yang, X. Ding, X. Ma, M. Zhang, One-dimensional CoP/MnO hollow nanostructures with enhanced oxygen evolution reaction activity, *J. Colloid Interface Sci.* 610 (2022) 663–670.
- [4] L. Liao, C. Cheng, H. Zhou, Y. Qi, D. Li, F. Cai, B. Yu, R. Long, F. Yu, Accelerating pH-universal hydrogen-evolving activity of a hierarchical hybrid of cobalt and dinickel phosphides by interfacial chemical bonds, *Mater. Today Phys.* 22 (2022), 100589.
- [5] T. Zhang, Y. Wang, J. Yuan, K. Fang, A. Wang, Heterostructured CoP@CoMoP nanocages as advanced electrocatalysts for efficient hydrogen evolution over a wide pH range, *J. Colloid Interface Sci.* 615 (2022) 465–474.
- [6] Y. Huang, M. Li, F. Pan, Z. Zhu, H. Sun, Y. Tang, G. Fu, Plasma-induced Mo-doped Co_3O_4 with enriched oxygen vacancies for electrocatalytic oxygen evolution in water splitting, *Carbon Energy* (2022) 1–14.
- [7] J. Luo, X. Wang, Y. Gu, D. Wang, S. Wang, W. Li, Y. Zhou, J. Zhang, Constructing hollow nanocages of Co_3O_4 -CoMoO₄ heterostructure for efficient electrocatalytic oxygen evolution reaction, *Appl. Surf. Sci.* 606 (2022), 154562.
- [8] Z. Xia, B. Deng, Y. Wang, Z. Jiang, Z. Jiang, Synergistic co-doping induced high catalytic activities of La/Fe doped Co_3O_4 towards oxygen reduction/evolution reactions for Zn-air batteries, *J. Mater. Chem. A* 10 (2022) 23483.
- [9] J. Chen, J. Zheng, W. He, H. Liang, Y. Li, H. Cui, C. Wang, Self-standing hollow porous Co/a-WO₃ nanowire with maximum Mott-Schottky effect for boosting alkaline hydrogen evolution reaction, *Nano Res.* (2022).

- [10] F. Gong, S. Ye, M. Liu, J. Zhang, L. Gong, G. Zeng, E. Meng, P. Su, K. Xie, Y. Zhang, J. Liu, Boosting electrochemical oxygen evolution over yolk-shell structured O-MoS₂ nanoreactors with sulfur vacancy and decorated Pt nanoparticles, *Nano Energy* 78 (2020), 105284.
- [11] X. Ren, F. Lyu, J. Yang, F. Wang, L. Xue, L. Wang, X. Zhang, Q. Wang, Homogeneous cobalt and iron oxide hollow nanocages derived from ZIF-67 etched by Fe species for enhanced water oxidation, *Electrochim. Acta* 296 (2019) 418–426.
- [12] L. Xia, L. Bo, W. Shi, Y. Zhang, Y. Shen, X. Ji, X. Guan, Y. Wang, J. Tong, Defect and interface engineering of templated synthesis of hollow porous Co₃O₄/CoMoO₄ with highly enhanced electrocatalytic activity for oxygen evolution reaction, *Chem. Eng. J.* 452 (2023), 139250.
- [13] S. Zhu, L. Huang, Z. He, K. Wang, J. Guo, S. Pei, H. Shao, J. Wang, Investigation of oxygen vacancies in Fe₂O₃/CoO_x composite films for boosting electrocatalytic oxygen evolution performance stably, *J. Electroanal. Chem.* 827 (2018) 42–50.
- [14] Y. Tong, K. Jin, H. Bei, J.Y.P. Ko, D.C. Pagan, Y. Zhang, F.X. Zhang, Local lattice distortion in NiCoCr, FeCoNiCr and FeCoNiCrMn concentrated alloys investigated by synchrotron X-ray diffraction, *Mater. Des.* 155 (2018) 1–7.
- [15] B. Zhang, J. Shan, W. Wang, P. Tsiakaras, Y. Li, Oxygen vacancy and core-shell heterojunction engineering of anemone-like CoP@CoOOH bifunctional electrocatalyst for efficient overall water splitting, *Small* 18 (2022) 2106012.
- [16] Q. Wang, H. Xu, X. Qian, G. He, H. Chen, Oxygen and sulfur dual vacancy engineering on a 3D Co₃O₄/Co₃S₄ heterostructure to improve overall water splitting activity, *Green Chem.* 24 (2022) 9220.
- [17] X. Wang, Y. Zhou, J. Luo, F. Sun, J. Zhang, Synthesis of V-doped urchin-like NiCo₂O₄ with rich oxygen vacancies for electrocatalytic oxygen evolution reactions, *Electrochim. Acta* 406 (2022), 139800.
- [18] Y. Li, Y. Wu, H. Hao, M. Yuan, S. Lv, L. Xu, B. Wei, In situ unraveling surface reconstruction of Ni₅P₄@FeP nanosheet array for superior alkaline oxygen evolution reaction, *Appl. Catal. B Environ.* 305 (2022), 121033.
- [19] B. Qiu, C. Wang, N. Zhang, L. Cai, Y. Xiong, Y. Chai, CeO₂-induced interfacial Co²⁺ octahedral sites and oxygen vacancies for water oxidation, *ACS Catal.* 9 (2019) 6484–6490.
- [20] D. Zheng, C. Gao, Z. Cheng, J. Zhou, X. Lin, L. Zhang, J. Wang, UCoO₄/Co₃O₄ heterojunction as a low-cost and efficient electrocatalyst for oxygen evolution, *Inorg. Chem.* 61 (2022) 19417–19424.
- [21] H. Li, X. Wu, P. Wang, S. Song, M. He, C. Li, W. Wang, Z. Fang, X. Yuan, W. Song, Z. Li, Interface engineering of hollow CoO/Co₃S₄@CoO/Co₃S₄ heterojunction for highly stable and efficient electrocatalytic overall water splitting, *ACS Sustain. Chem. Eng.* 10 (2022) 13112–13124.
- [22] Y. Li, Y. Li, Y. Wu, M. Yuan, H. Hao, Z. Lv, L. Xu, B. Wei, Operando spectroscopies unveil interfacial FeOOH induced highly reactive β-Ni(Fe)OOH for efficient oxygen evolution, *Appl. Catal. B Environ.* 318 (2022), 121825.
- [23] Y. Ma, K. Wang, Y. Chen, X. Yang, S. Zhao, K. Xi, S. Xie, S. Ding, C. Xiao, Galvanic exchange carving growth of Co-Fe LDHs with enhanced water oxidation, *Int. J. Hydrog. Energ.* 44 (2019) 20085–20092.
- [24] Q. Niu, M. Yang, D. Luan, N. Li, L. Yu, X. Lou, Construction of Ni-Co-Fe hydr(oxy) oxide@Ni-Co layered double hydroxide yolk-shelled microrods for enhanced oxygen evolution, *Angew. Chem. Int. Ed.* 61 (2022), e202213049.
- [25] J. Xie, Z. Liu, J. Li, L. Feng, M. Yang, Y. Ma, D. Liu, L. Wang, Y. Chai, B. Dong, Fe-doped CoP core-shell structure with open cages as efficient electrocatalyst for oxygen evolution, *J. Energy Chem.* 48 (2020) 328–333.
- [26] W. Liu, H. Liu, L. Dang, H. Zhang, X. Wu, B. Yang, Z. Li, X. Zhang, L. Lei, S. Jin, Amorphous cobalt-iron hydroxide nanosheet electrocatalyst for efficient electrochemical and photo-electrochemical oxygen evolution, *Adv. Funct. Mater.* 27 (2017) 1603904.
- [27] X. Ding, H. Huang, Q. Wan, X. Guan, Y. Fang, S. Lin, D. Chen, Z. Xie, Self-template synthesis of hollow Fe-doped CoP prisms with enhanced oxygen evolution reaction activity, *J. Energy Chem.* 62 (2021) 415–422.
- [28] X. Wei, Y. Zhang, B. Zhang, Z. Lina, X. Wang, P. Hu, S. Lia, X. Tan, X. Cai, W. Yang, L. Mai, Yolk-shell-structured zinc-cobalt binary metal sulfide@N-doped carbon for enhanced lithium-ion storage, *Nano Energy* 64 (2019), 103899.
- [29] G. Gong, J. Zhu, J. Li, R. Gao, Q. Zhou, Z. Zhang, H. Dou, L. Zhao, X. Sui, J. Cai, Y. Zhang, B. Liu, Y. Hu, A. Yu, S. Sun, Z. Wang, Z. Chen, Self-templated hierarchically porous carbon nanorods embedded with atomic Fe-N₄ active sites as efficient oxygen reduction electrocatalysts in Zn-air batteries, *Adv. Funct. Mater.* 31 (2021) 2008085.
- [30] C. Sun, W. Chen, P. Gao, H. Hu, J. Zheng, Y. Zhu, Investigation of structure and cycling performance of Nb-doped nickel-rich single-crystal ternary cathode materials, *Ionics* 28 (2021) 747–757.
- [31] Y. Dang, P. Han, Y. Li, Y. Zhang, Y. Zhou, Low-crystalline mixed Fe-Co-MOFs for efficient oxygen evolution electrocatalysis, *J. Mater. Sci.* 55 (2020) 13951–13963.
- [32] P. Tan, B. Chen, H. Xu, W. Cai, W. He, M. Chen, M. Ni, Synthesis of Fe₂O₃ nanoparticle-decorated N-doped reduced graphene oxide as an effective catalyst for Zn-air batteries, *J. Electrochem. Soc.* 166 (2019) A616–A622.
- [33] G. Gnanamoorthy, V. Karthikeyan, D. Ali, G. Kumar, S.G. Jenifer, V.K. Yadav, N. Choudhary, V. Narayanan, Realization of rGO/ZnCo₂O₄ nanocomposites enhanced for the antimicrobial, electrochemical and photocatalytic activities, *Diam. Relat. Mater.* 120 (2021), 108677.
- [34] H. Chu, D. Zhang, P. Feng, Y. Gu, P. Chen, K. Pan, H. Xie, M. Yang, Engineering oxygen vacancies in CoO@Co₃O₄/C nanocomposites for enhanced electrochemical performances, *Nanoscale* 13 (2021) 19518.
- [35] Y. Zhang, T. Lu, Y. Ye, W. Dai, Y. Zhu, Y. Pan, Stabilizing oxygen vacancy in entropy-engineered CoFe₂O₄-type catalysts for co-prosperity of efficiency and stability in an oxygen evolution reaction, *ACS Appl. Mater. Interfaces* 12 (2020) 32548–32555.
- [36] L. Zhang, C. Lu, F. Ye, Z. Wu, Y. Wang, L. Jiang, L. Zhang, C. Cheng, Z. Sun, L. Hu, Vacancies boosting strategy enabling enhanced oxygen evolution activity in a library of novel amorphous selenite electrocatalysts, *Appl. Catal. B Environ.* 284 (2021), 119758.
- [37] W. Gou, Z. Xia, X. Tan, Q. Xue, F. Ye, S. Dai, M. Zhang, R. Si, Y. Zou, Y. Ma, J.C. Ho, Y. Qu, Highly active and stable amorphous IrO_x/CeO₂ nanowires for acidic oxygen evolution, *Nano Energy* 104 (2022), 107960.
- [38] V. Ganesan, J. Son, J. Kim, CoP₂/Fe-CoP₂ yolk-shell nanoboxes as efficient electrocatalysts for the oxygen evolution reaction, *Nanoscale* 13 (2021) 4569.
- [39] X. Wang, L. Yu, B. Guan, S. Song, X. Lou, Metal-organic framework hybrid-assisted formation of Co₃O₄/Co-Fe oxide double-shelled nanoboxes for enhanced oxygen evolution, *Adv. Mater.* 30 (2018) 1801211.
- [40] P. Gao, Y. Zeng, P. Tang, Z. Wang, J. Yang, A. Hu, J. Liu, Understanding the synergistic effects and structural evolution of Co(OH)₂ and Co₃O₄ toward boosting electrochemical charge storage, *Adv. Funct. Mater.* 32 (2022) 2108644.
- [41] X. Li, Q. Zha, Y. Ni, Ni-Fe phosphate/Ni foam electrode: facile hydrothermal synthesis and ultralong oxygen evolution reaction durability, *ACS Sustain. Chem. Eng.* 7 (2019) 18332–18340.
- [42] C. Bai, L. Hong, Z. Chong, L. Bao, L. Di, Visible light induced photocatalytic activity of ZnCo₂O₄ nanoparticles, *Acta Phys. Chim. Sin.* 27 (2011) 2411–2415.
- [43] O.D. Morales, D.F. Suspedra, M.T.M. Koper, The importance of nickel oxyhydroxide deprotonation on its activity towards electrochemical water oxidation, *Chem. Sci.* 7 (2016) 2639.
- [44] E.L. Uzunova, H. Mikosch, G.S. Nikolov, Electronic structure of oxide, peroxide, and superoxide clusters of the 3d elements: a comparative density functional study, *J. Chem. Phys.* 128 (2008), 094307.
- [45] B.J. Trześniewski, O.D. Morales, D.A. Vermaas, A. Longo, W. Bras, M.T.M. Koper, W.A. Smith, In situ observation of active oxygen species in Fe-containing Ni-based oxygen evolution catalysts: the effect of pH on electrochemical activity, *J. Am. Chem. Soc.* 137 (2015) 15112–15121.
- [46] Q. Yang, Z. Lu, J. Liu, X. Lei, Z. Chang, L. Luo, X. Sun, Metal oxide and hydroxide nanoarrays: Hydrothermal synthesis and applications as supercapacitors and nanocatalysts, *Prog. Nat. Sci.* 23 (2013) 351–366.
- [47] Q. Yang, S. Cheng, C. Yang, Z. Lei, Vertically grown p-n heterojunction FeCoNi LDH/CuO arrays with modulated interfacial charges to facilitate the electrocatalytic oxygen evolution reaction, *J. Mater. Chem. A* 10 (2022) 11938–11947.
- [48] Y. Zhou, R. Fan, Y. Cao, H. Wang, B. Dong, H. Zhao, F. Wang, J. Yu, Y. Chai, Oriented and robust anchoring of Fe via anodic interfacial coordination assembly on ultrathin Co hydroxides for efficient water oxidation, *Nanoscale* 13 (2021) 13463.
- [49] M. Cai, Q. Zhu, X. Wang, Z. Shao, L. Yao, H. Zeng, X. Wu, J. Chen, K. Huang, S. Feng, Formation and stabilization of NiOOH by introducing α-FeOOH in LDH: composite electrocatalyst for oxygen evolution and urea oxidation reactions, *Adv. Mater.* 35 (2022) 2209338.
- [50] X. Duan, S. Ren, N. Pan, M. Zhang, H. Zheng, MOF-derived Fe₂Co@N-C bifunctional oxygen electrocatalysts for Zn-air batteries, *J. Mater. Chem. A* 00 (2020) 1–3.